PROCEEDINGS OF SCIENCE

Home | what's PoS | for organizers | for chairpersons | for authors | for readers | staff

Volume 501 - 39th International Cosmic Ray Conference (ICRC2025) - Plenary talks

Exploring the Ultra-High-Energy Universe: Highlights from the Pierre Auger Observatory

The Pierre Auger Collaboration, A. Abdul Halim, P. Abreu, M. Aglietta, I. Allekotte, K. Almeida Cheminant, et al. (click to show)

*: corresponding author

Full text: pdf

Abstract

The Pierre Auger Observatory is the world's largest facility dedicated to studying ultra-high-energy cosmic rays (UHECRs). Located in Argentina, it spans 3,000 square kilometers and utilizes a hybrid detection system comprising over 1,600 Water-Cherenkov detectors and fluorescence telescopes. Since its inception in 2004, the Observatory has provided groundbreaking insights into the energy spectrum, mass composition, and arrival direction anisotropies of cosmic rays.
Phase-I data analysis, covering the years 2004-2022, has revealed critical features such as large-scale anisotropies and spectral features such as the instep and the suppression of flux at the highest energies, thus advancing our understanding of the origin and propagation of UHECRs. The hybrid detection approach has enabled precise measurements of air showers and muon content, offering constraints on hadronic interaction models. Furthermore, searches for neutral particles have been performed, contributing to multi-messenger astrophysics.
The ongoing AugerPrime upgrade aims to refine mass composition studies by integrating scintillator detectors, improved electronics, underground muon detectors, and radio antennas, enhancing sensitivity to primary cosmic-ray properties. We present the key scientific achievements from Phase I and discuss the transformative potential of AugerPrime in addressing fundamental questions about the origin of UHECRs.

How to cite

Metadata are provided both in *article* format (very similar to INSPIRE) as this helps creating very compact bibliographies which can be beneficial to authors and readers, and in *proceeding* format which is more detailed and complete.

Open Access

Exploring the Ultra-High-Energy Universe: Highlights from the Pierre Auger Observatory

Markus Roth[a,*] **for the Pierre Auger Collaboration**[b]

[a]*Institute for Astroparticle Physics, Karlsruhe Institute of Technology* ◣**KIT**, *Karlsruhe, Germany*

[b]*Observatorio Pierre Auger, Av. San Martín Norte 304, 5613 Malargüe, Argentina*
Full author list: https://www.auger.org/archive/authors_icrc_2025.html

E-mail: spokespersons@auger.org

The Pierre Auger Observatory is the world's largest facility dedicated to studying ultra-high-energy cosmic rays (UHECRs). Located in Argentina, it spans 3,000 square kilometers and utilizes a hybrid detection system comprising over 1,600 Water-Cherenkov detectors and fluorescence telescopes. Since its inception in 2004, the Observatory has provided groundbreaking insights into the energy spectrum, mass composition, and arrival direction anisotropies of cosmic rays. Phase-I data analysis, covering the years 2004-2022, has revealed critical features such as large-scale anisotropies and spectral features such as the instep and the suppression of flux at the highest energies, thus advancing our understanding of the origin and propagation of UHECRs. The hybrid detection approach has enabled precise measurements of air showers and muon content, offering constraints on hadronic interaction models. Furthermore, searches for neutral particles have been performed, contributing to multi-messenger astrophysics. The ongoing AugerPrime upgrade aims to refine mass composition studies by integrating scintillator detectors, improved electronics, underground muon detectors, and radio antennas, enhancing sensitivity to primary cosmic-ray properties. We present the key scientific achievements from Phase I and discuss the transformative potential of AugerPrime in addressing fundamental questions about the origin of UHECRs.

*Speaker

1. Introduction

Studying ultra-high-energy cosmic rays (UHECRs) with energies exceeding 10^{17} eV opens up an intriguing possibility: to shed light on some of the most powerful phenomena in the universe. However, more than a century after Victor Hess's pioneering discovery of cosmic rays, the origin of these extraordinary particles remains unknown. This mystery persists because, despite increasingly precise measurements, the arrival directions of UHECRs exhibit only weak correlations with known astrophysical structures. The naive approach of identifying sources based on direction, which is so successful in photon astronomy, poses an extremely challenging task when it comes to charged particles. Galactic magnetic fields deflect these particles significantly during their propagation. As a result, their paths become scrambled, obscuring the true locations of their sources. While a comprehensive framework that fully explains the production environments, acceleration mechanisms, and detailed composition of UHECRs is still lacking, remarkable progress has been achieved in recent years. Much of this progress is due to the unprecedented data gathered by the Pierre Auger Observatory. The Observatory has collected the largest ever dataset of UHECR events, providing an exceptional statistical basis for improving our understanding. These observations reveal a surprisingly sophisticated global picture that challenges many long-standing assumptions. One of the most striking results concerns the behaviour of the primary composition, which becomes progressively heavier above energies close to the ankle. As energy increases, distinct mass groups appear to replace one another, leading to a scenario in which each energy band is dominated by a particular nuclear group. This evolution overturns earlier models that relied on a proton-only composition to explain both the ankle [1] and the high-energy suppression [2, 3]. Interpreting these findings requires the use of hadronic interaction models, which must be extrapolated to energies far beyond the reach of current particle accelerators. In this extreme regime, UHECRs themselves act as unique probes of fundamental physics. Measurements at the Pierre Auger Observatory have demonstrated a significant excess of muons [4–8], which relative to the predictions of the most recent hadronic interaction models is now of the order of 20%. This discrepancy signals that our understanding of hadronic physics at ultra-high energies is still incomplete. To address these challenges and enhance composition sensitivity, the Observatory underwent a major upgrade known as AugerPrime [9]. This upgrade marks the transition from Phase I to Phase II of the facility's scientific mission. AugerPrime will greatly strengthen the ability to disentangle the mass composition across the entire energy range. This paper highlights the state of the upgrade and the latest findings obtained using the Phase-I data from the Observatory. Further, recently published conference overview articles with slightly different focuses expand on and deepen aspects that are only touched upon here [10, 11].

2. The Pierre Auger Observatory

The Pierre Auger Observatory, the layout of which is shown schematically in Fig. 1 (left), is located in the vicinity of Malargüe in Argentina. The Surface Detector (SD) is composed of an array of approximately 1,660 Water-Cherenkov detectors (WCDs), arranged in a grid over an area of about 3,000 km² (Fig. 1, right). These detectors are used to detect particles in extensive air showers (EASs) as they travel towards the ground, as well as to measure the distribution of their
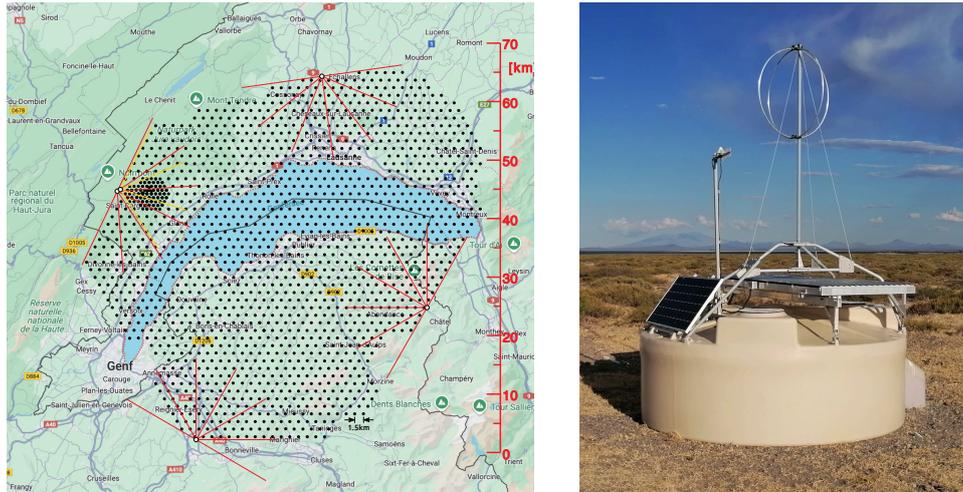
Figure 1: On the left a layout of the Pierre Auger Observatory, displaying the positions of the WCDs (black dots) and the azimuthal field of view of the FD telescopes (red and orange lines). Lake Geneva, near where the conference took place, is superimposed in the background, giving an impression of the size of the Observatory. On the right a WCD station equipped with AugerPrime detectors. The SSD is positioned on top of the WCD, with the radio antenna placed on top of the SSD.

arrival times. The Fluorescence Detector (FD) comprises 24 telescopes that span an elevation range of 3 to 30 degrees, arranged in four sites. The energy deposited in the atmosphere is measured through the fluorescence light produced during the development of the EAS. A variety of devices are utilised for the purpose of monitoring the atmosphere. Two additional, denser arrays of WCDs are installed with spacings of 750 m and 433 m, in addition to three High-Elevation Fluorescence Telescopes (HEAT). The elevation angle of these telescopes ranges from 30 to 60 degrees; this is required to extend the energy range down to approximately $10^{16.5}$ eV. The Auger Engineering Radio Array (AERA), which consists of over 150 radio antennas, measures low energy showers by detecting their radio emission. In addition to its scientific mission, the construction and operation of the Observatory has had a deep social, economic, educational, and cultural impact on the local community, the region, and beyond [12].

2.1 The upgrade AugerPrime

The AugerPrime upgrade [13] aims to improve the mass sensitivity of the surface detector array by adding complementary detector systems to the existing Water-Cherenkov Detectors. This enhancement is achieved through the installation of Scintillator Surface Detectors (SSDs) and radio antennas, collectively known as the Radio Detector (RD) (see Fig. 1, right). Both systems are mounted atop the existing 1500 m–spaced WCD array that covers 3,000 km^2. The SSDs provide a response distinct from that of the WCDs to the electromagnetic and muonic components of extensive air showers. This difference enables a deconvolution of shower components or the integration of time-dependent detector signals into advanced reconstruction algorithms. For air showers with zenith angles $\theta \geq 60°$, the electromagnetic component becomes strongly attenuated, reducing the effectiveness of the SSD measurements. At such high inclinations, the radio footprint of the showers becomes sufficiently large to enable accurate energy estimation through radio sampling. Once the
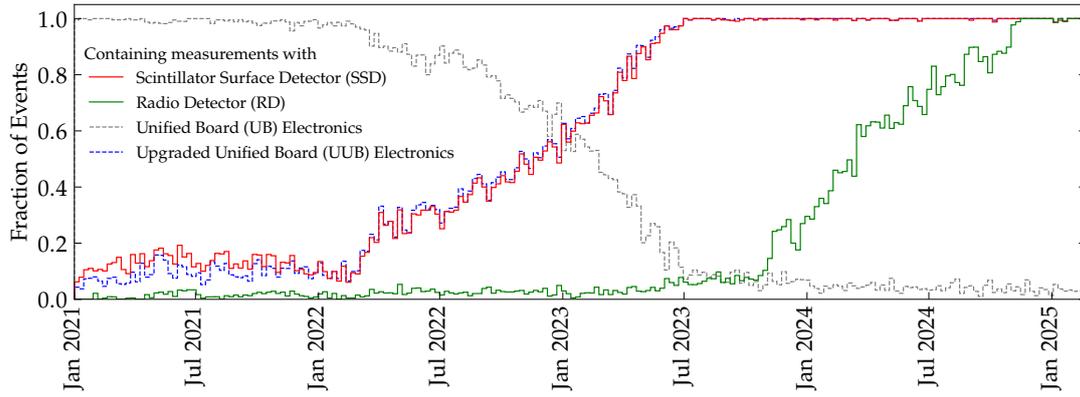
Figure 2: Fraction of events with energies greater than $10^{18.5}$ eV containing measurements with the different detector components of the AugerPrime upgrade during the transition period [9].
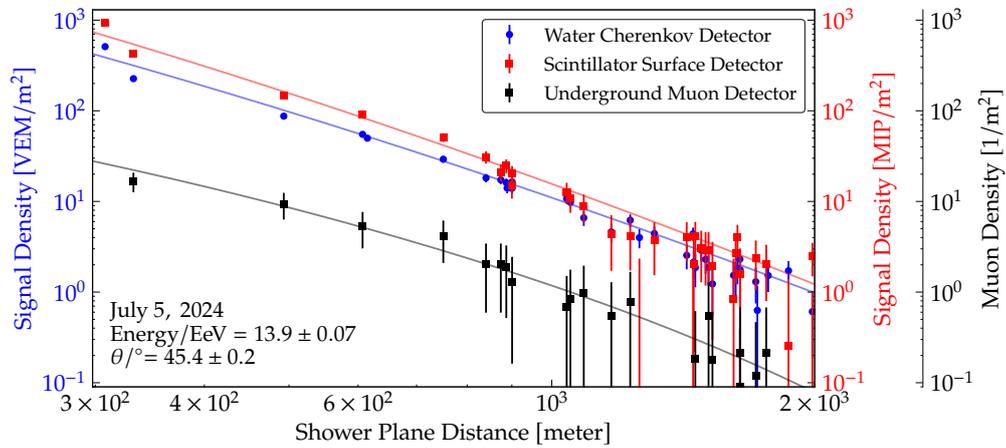
Figure 3: Lateral distributions of signals from the Water-Cherenkov Detectors, Scintillator Surface Detectors and the Underground Muon Detector shown for an event of Phase II [9].

energy is determined from radio measurements, the WCDs can provide mass-sensitive information for inclined showers. Thus, the combination of SSDs and radio antennas yields mass sensitivity over nearly the entire sky observed by the Observatory. Less inclined showers rely primarily on scintillator information, whereas more inclined showers depend on radio measurements. The $20\,\mathrm{km}^2$ region of the array with $750\,\mathrm{m}$ spacing is being enhanced with additional underground scintillation detectors. The yet denser $2\,\mathrm{km}^2$ sub-array within this region, featuring $433\,\mathrm{m}$ spacing, is also equipped with these detectors. These buried scintillators, termed the Underground Muon Detector (UMD), provide direct measurements of muons in showers with zenith angles up to about $60°$. The UMD yields high-precision muon data for cosmic rays with energies spanning from the second knee to the ankle of the spectrum. Furthermore, its direct muon measurements will calibrate the algorithms used to estimate muon content in the upgraded $3{,}000\,\mathrm{km}^2$ array. A more detailed description of the AugerPrime detectors and their potential scientific output can be found in [9].

Deployment of the various detectors started in early 2021 and was mostly finished by late 2024
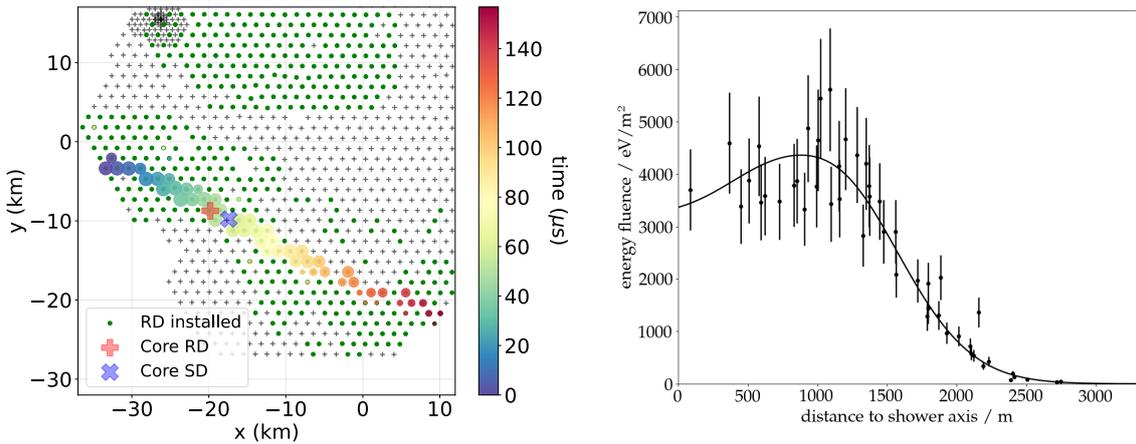
Figure 4: On the left-hand side the topology and on the right-hand side the lateral distribution of energy fluence is shown for an inclined event sample, measured using the Phase-II Radio Detector ($E = 32\,\mathrm{EeV}$, $\theta = 84.8°$) [9].

(see Fig. 2). During this transitional period, the process of collecting data had smoothly evolved from older to newer electronics, including the additional detectors. At the time of these proceedings, the exposure of the Phase-II surface detector is already close to 10% of that of the Phase-I detector. Fig. 3 illustrates an event at a moderate zenith angle of about 45°, where the additions alongside the WCD data by means of SSD and UMD data are shown. The deployment of RD commenced in August 2023 and was finished at the close of 2024. Each RD antenna was immediately put into a data acquisition mode upon its deployment. An illustrative event measured during the RD deployment is presented in Fig. 4.

3. Physics results of Phase I

The data of Phase I from the Pierre Auger Observatory are exceptionally impressive providing the world's largest database of events at extreme energies [14]. The following section will provide an update on the most notable results presented by the Pierre Auger Collaboration at this conference.

3.1 The energy spectrum of UHECRs

The Water-Cherenkov detectors possess sufficient depth of 1.2 m to measure particles arriving at large zenith angles. However, the structure of extensive air showers varies substantially between vertical and inclined geometries. More vertical showers remain approximately symmetric around their axis and retain significant photon and electron content at ground level. In contrast, inclined showers are dominated by muons and lose axial symmetry due to geomagnetic effects and other influences. Because of these differences, events with zenith angles up to 60° are reconstructed using a method distinct from that for events between 60° and 80°. For vertical events, a function describing the fall-off of WCD signals with distance from the shower axis is employed as shown in Fig. 3. The value of this function at 1000 m, denoted $S(1000)$, acts as an estimator of the shower size. To remove zenith-angle dependence, an angle-corrected size parameter is defined. This parameter, S_{38}, corresponds to the size the shower would have had if observed at a zenith angle of 38°. It is
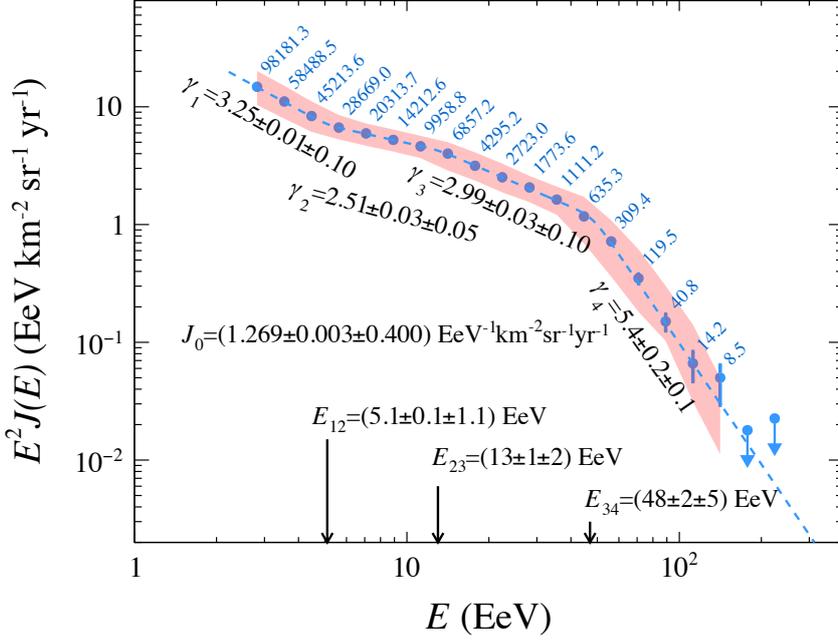
Figure 5: The energy spectrum scaled by E^2 across the declination range $[-90°, +44.8°]$ [15, 16]. The number of events corrected for detector effects is shown in each bin. The red band represents the systematic uncertainties, and the dashed line represents the best-fit function described by the spectral features, which are given with their statistical and systematic uncertainties.

obtained through an attenuation function derived using the Constant Intensity Cut method. The S_{38} shower size is calibrated using the energy measured by the Fluorescence Detector telescopes, E_{FD}, for high-quality events registered also by by the Surface Detector array in coincidence, utilizing the formula $E = A S_{38}^B$, with $A = (186 \pm 3)$ PeV, $B = 1.021 \pm 0.004$, and resulting in a correlation coefficient between A and B of $\rho = -0.98$. A similar procedure has been invoked for the inclined events as well as to provide a data driven energy estimate from fluorescence data [15, 16]. The combined spectrum and the corresponding fit including fitted parameters are shown in Fig. 5, and the spectrum data are provided in [15]. The shaded band represents the systematic uncertainty of the flux, which is dominated by the 14% systematic uncertainty of the energy scale. The flux exhibits the firmly established features of the ankle and suppression, as well as the instep, which we unveiled with a significance of 3.9σ in 2020 [17] and meanwhile increased to 5.5σ.

The Observatory's latitude of 35.2° S allows to use vertical events to probe declinations from the south celestial pole up to +24.8°, while inclined events extend this range to $[-84.8°, +44.8°]$. A search for declination dependence was performed by dividing the sky into five declination bands, including four bands within the vertical-event range and an additional northern band observed only with inclined events. For each band, a combined spectrum was computed and compared with the reference flux in the common declination interval of both data sets. The resulting spectra and reference are shown in Fig. 6, together with the expected modulated flux arising from the dipole anisotropy measured by Auger. The residuals exhibit a dipole-imprinted trend between 4 and 32 EeV, while at higher energies, statistical uncertainties dominate. To state it explicitly, no
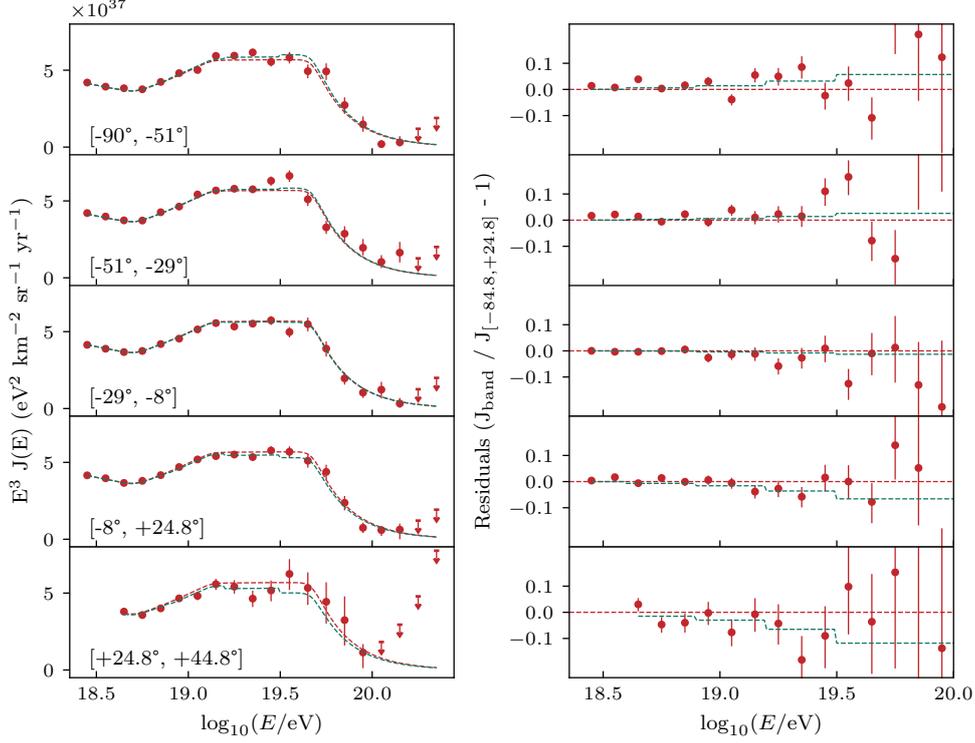
Figure 6: Left: Energy spectra in five declination ranges [15, 16]. The red dashed reference lines show the best-fit function for the common spectrum $[-84.8°, +24.8°]$. The green dashed lines account for the impact of dipole anisotropies in each band. Right: Corresponding residuals and expectations.

statistically significant dependence of the flux with declination from the south celestial pole up to $+44.8°$ has been found, apart from the minor trend that is consistent with the well-established dipolar anisotropy in arrival directions. The quasi-uniformity of the spectra across declination disfavors the new spectral feature arising from a few sources having different characteristics

3.2 The mass composition of UHECRs and its interplay with hadronic interactions

A notable finding is the intricate evolution of the mass composition of ultra-high-energy cosmic rays (UHECRs), as evidenced by a thorough examination of quantities such as the depth of shower maximum, X_{max}. Through the collection of more data and the employment of increasingly sophisticated analytical techniques, more detailed information is being revealed, thereby enhancing the robustness of the general picture of UHECR mass composition.

Due to significant shower-to-shower fluctuations, X_{max} cannot be used reliably to determine the mass of a primary cosmic ray on an event-by-event basis. Instead, X_{max} measurements within a narrow energy interval are combined into distributions whose statistical moments provide estimates of the average mass composition. Since the most recent reporting of combined X_{max} measurements [18], the Phase-I FD hybrid X_{max} analysis has been completed, and a Universality-based SD reconstruction as well as an SD DNN reconstruction have been performed (see Ref. [8] for more details). A detailed description of the Universality method and its results is provided in separate proceedings [19]. The updated FD hybrid analysis [20] significantly enhances both statistics and
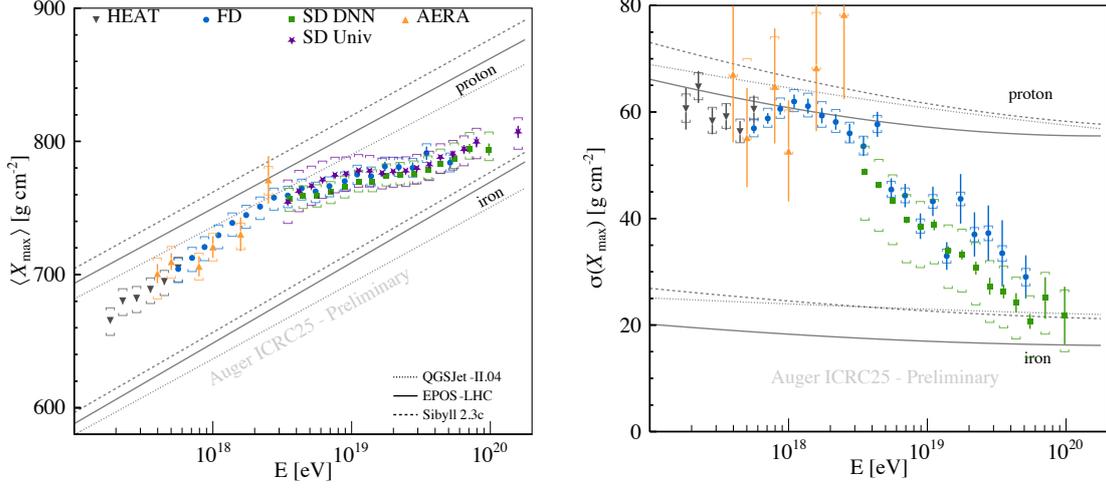
Figure 7: The mean (left) and the standard deviation (right) of X_{max} distributions measured with the FD [22], the SD [23, 28], and AERA [25] during Phase I. Preliminary measurements from HEAT [27] are also shown.

methodology, resulting in a Phase-I dataset containing more than twice the number of events used in the initial publication from 2014 [21] and enabling additional energy bins at both low and high energies. Because the DNN-based SD X_{max} analysis was calibrated using the older FD hybrid reconstruction to remove dependencies on the hadronic interaction model used for training, it consequently inherits the previous FD X_{max} scale, including the resulting ~ 5 g/cm^2 offset, while the Universality approach is calibrated by means of the current FD data.

The most recent measurements of $\sigma(X_{max})$ agree with the 2014 FD results, but a discrepancy appears when compared with the SD DNN, which is likely attributable to the larger SD systematic uncertainties of about 10 g/cm^2 and remaining model or methodological dependencies [22, 23]. A comprehensive summary of the latest X_{max} measurements from FD Hybrid [24], SD [19, 23], and AERA [25, 26], along with preliminary HEAT results [27], is presented in Fig. 7. Despite updates to reconstruction methods across FD, HEAT, AERA, and SD datasets, the measured values of $\langle X_{max} \rangle$ remain highly consistent over all energies. The behavior of $\sigma(X_{max})$ is more intricate, with the hybrid data showing an outlier in the energy bin $\log_{10}(E/\text{eV}) \in [18.6, 18.7]$ whose removal would reduce $\sigma(X_{max})$ by about 2 g/cm^2 and better align it with the overall trend. Furthermore, $\sigma(X_{max})$ from the SD Universality method is not shown due to ongoing resolution corrections.

The moments of X_{max} already convey substantial information about the mass composition of UHECRs, but additional processing is required to obtain a more comprehensive understanding. One useful strategy is to convert the moments of X_{max} into moments of $\ln A$, following the method of Ref. [29], while another involves fitting the fractional contributions of different mass groups using the measured X_{max} distributions in each energy bin [30]. The transformation of $\langle X_{max} \rangle$ and $\sigma(X_{max})$ into $\langle \ln A \rangle$ and its variance $V(\ln A)$ relies on hadronic interaction models to set the X_{max} scale and describe its intrinsic fluctuations. These conversions introduce model-dependent quantities such as the proton and iron nuclei expectations for X_{max}, the variance associated with shower development, and further parameters, which appear in the formalism. Applying this procedure to FD, SD–DNN, and HEAT data with EPOS-LHC [31], Sibyll 2.3d [32], and QGSJet-II.04 [33]
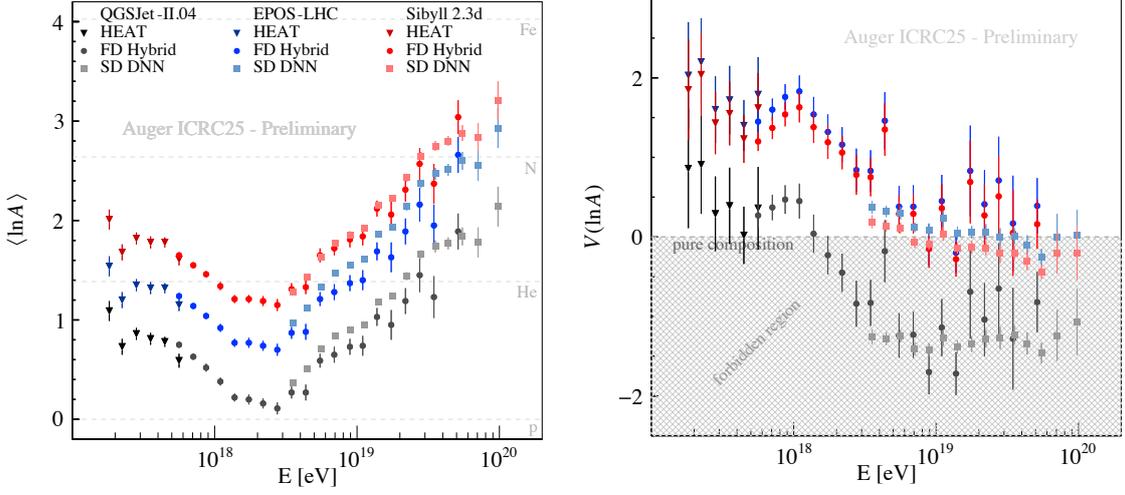
Figure 8: The first raw and second central moments of the ln A distributions obtained from the FD [24] and SD Phase-I [23] X_{max} data shown in Fig. 7, using the hadronic interaction models QGSJet-II.04 (grey) [33], EPOS-LHC (blue) [31], and Sibyll 2.3d (red) [32]. These model-dependent transformations illustrate how different hadronic interaction models map the observed X_{max} moments into corresponding mass-composition moments.

yields the corresponding moments of ln A shown in Fig. 8. Although these moments effectively summarize the average composition, they do not directly reveal the contributions from individual mass groups. To extract such information, templates of the X_{max} distributions for protons, helium, nitrogen, and iron nuclei are generated using hadronic interaction models and fitted to the observed distributions in each energy bin. This fitting procedure has been applied to both the hybrid FD dataset of Phase-I and preliminary HEAT measurements, as illustrated in Fig. 9. An extension to this method allows for estimating the proton-air cross-section as discussed in [34]. The resulting estimates depend strongly on the chosen hadronic interaction models, and continuing developments in these models are expected to modify both the X_{max} scale and its energy dependence. Despite these uncertainties, additional complementary techniques, such as comparisons of SD signals sensitive to X_{max} and detailed studies of the energy evolution of $\langle X_{max} \rangle$ and $\sigma(X_{max})$, help clarify trends without relying entirely on hadronic models. When all available methods and datasets from Phase I are synthesized, they collectively support a consistent picture of UHECR mass composition across the accessible energy range. Above $10^{17.2}$ eV, the composition is predominantly hadronic, exhibits a non-monotonic evolution with a minimum near 3 EeV, shows structured changes in X_{max} with energy, and becomes progressively less mixed at the highest energies, where narrow mass groups increasingly dominate the flux. In addition to the previously reported muon deficit using, for example, inclined air showers in the prediction of hadronic interaction generators [4], vertical showers are also used to identify deficits in simulations.

The combined Surface and Fluorescence Detectors enable testing of hadronic interaction models using the method described in Ref. [35], with the most recent updates to hadronic generators presented at this conference (EPOS-LHC-R, QGSJet-III-01 and SIBYLL-2.3e) incorporated.
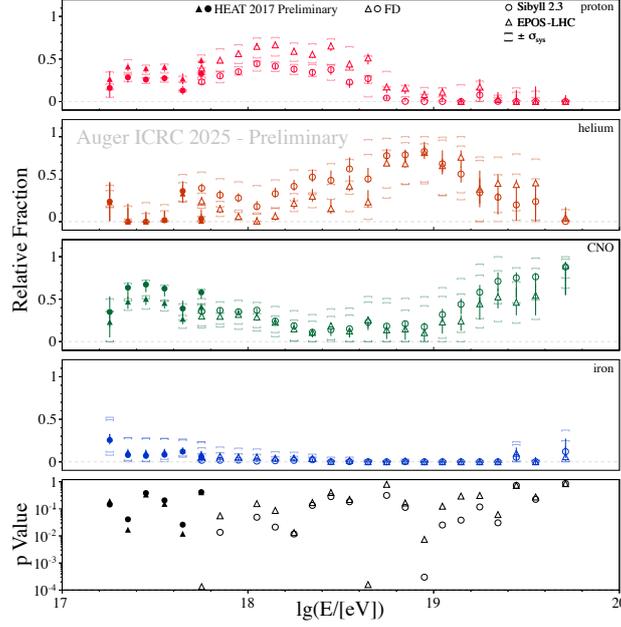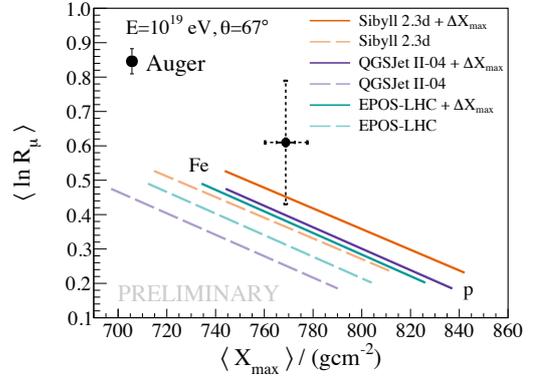
Figure 9: The fractional mass composition of UHECRs from FD [24] and preliminary HEAT [27] data is estimated using Sibyl 2.3 (HEAT), Sibyl 2.3d, and EPOS-LHC, while QGSJet-II.04 is excluded due to unphysical results. Further details on the analysis methods and updated model fits can be found in [22, 24].

The model predictions are assumed to be adjustable by two mass- and energy-independent parameters: $\Delta X_{\max}$, which uniformly shifts the predicted depth of shower maximum, and $R_{\mathrm{had}}(\theta)$, which rescales the hadronic component of the ground signal measured at $1000\,\mathrm{m}$ from the shower core. These corrections allow us to phenomenologically tune simulations to better match the data, without requiring changes to the underlying hadronic interaction physics.

Although improvements in the description of the measured $\langle X_{\max} \rangle$ scale are visible in these recent versions of EPOS and QGSJet, all models still fail to fully reproduce the data in the inspected range from $10^{18.5}$ to $10^{19.0}$ eV and results in extreme cases to values of $R_{\mathrm{had}}(\theta) \simeq 1.3$ and $\Delta X_{\max} \simeq 28 \mathrm{g/cm^2}$. Each model predicts a muon spectrum that is too hard, resulting in less steep attenuation of the hadronic signal than what the experimental data favors.

Interestingly, the inferred primary mass composi-

Figure 10: The muon scale R_μ versus $X_{\max}$ measurement at the Pierre Auger Observatory using inclined showers at about $10\,\mathrm{EeV}$, following Ref. [7], is shown together with predictions between proton and iron nuclei for both the original hadronic interaction models (dashed lines) and their $X_{\max}$-shifted counterparts (solid lines).

tion remains consistent across model generations when $\Delta X_{\max}$ and $R_{\mathrm{had}}(\theta)$ corrections are applied, suggesting a robust phenomenological description despite underlying model flaws. No significant energy dependence in these modifications was found in this energy range, allowing us to extrapolate
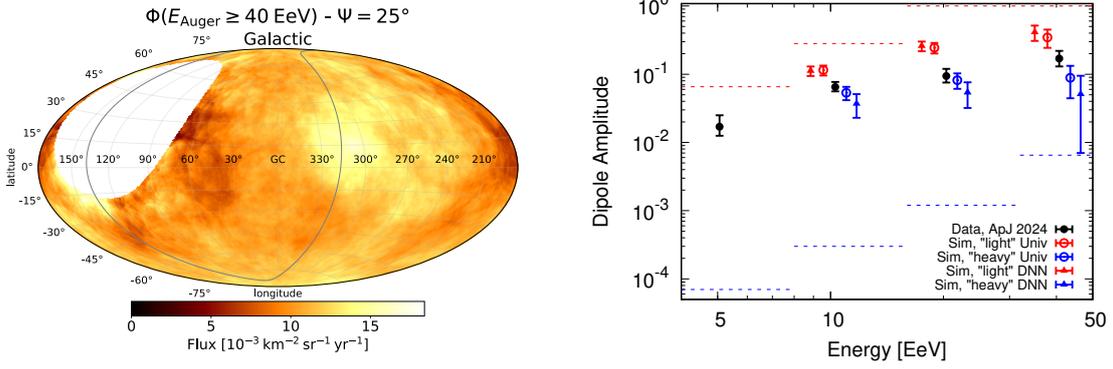
Figure 11: Left: Flux map at energies above 40 EeV filtered with a top-hat smoothing radius of $\Psi = 25°$ in Galactic coordinates [36]. The supergalactic plane is shown as a grey line. The blank area falls outside the Pierre Auger Observatory's field of view. Right: Black circles represent the dipole amplitudes measured from data. Expected dipole amplitude as a function of energy shown for "light" (red) and "heavy" (blue) mass groups using universality-based mass estimators (open circles) and deep-learning estimators (DNN, filled triangles). Predicted amplitudes for proton and iron primaries are indicated by the red and blue dashed lines, respectively.

model predictions across the full range and examine spectral features like the ankle and instep.

Under a constant ΔX_{max} correction, the proton and helium fractions are suppressed above the ankle, the nitrogen peaks near the instep, and the iron component rises towards the highest energies, indicating a progressively heavier composition at the highest energies. Fig. 10 illustrates the mitigation of the muon deficit for the measurements of [7] at zenith angles $62° \leq \theta \leq 80°$, by shifting the original model predictions (dashed lines) according to the ΔX_{max} values obtained in [35]. After this correction, the models underestimate the muon scale by only 15–25%, which is consistent with the values reported in [8, 35] for $\theta \leq 60°$. The updated EPOS-LHC-R model predicts a larger muon yield at high zenith angles, thereby improving the agreement with the measured muon size in inclined showers. This reinforces the idea that, although progress is being made, there is still a need for fundamental improvements in hadronic interaction modelling.

3.3 Arrival Directions of UHECRs

The Auger Observatory conducts numerous searches for small- and intermediate-scale aniso-tropies using methods such as localised excess searches, autocorrelation studies, and correlations with large-scale structures. Likelihood-ratio analyses comparing UHECR arrival directions with flux patterns expected from astrophysical catalogs by contrasting against isotropy reveal the strongest correlation for starburst galaxies. Catalog-based searches and searches focused on the Centaurus region both indicate that the most significant signals arise above an energy threshold of approxi-mately 40 EeV as seen in Fig. 11 (left) [36]. The clearest evidence for an extragalactic origin of UHECRs above 8 EeV arises from the large-scale dipole, whose direction lies 113° away from the Galactic center [37]. The dipole amplitude increases with energy, likely due to a combination of a more prominent contribution from nearby, anisotropically distributed sources and the rise of the average primary mass (see Fig. 11, right). When astrophysical scenarios inferred from the energy spectrum and mass composition are considered, the observed dipole amplitude is compatible with
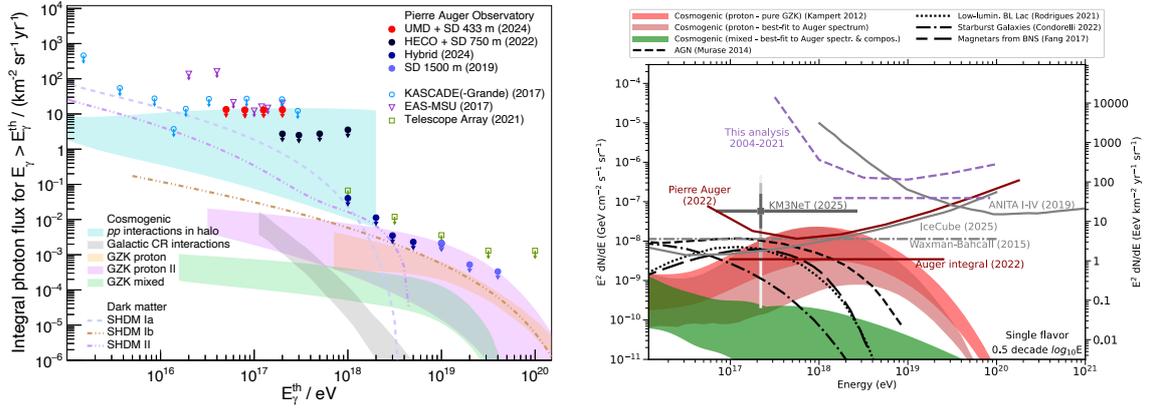
Figure 12: Left: 95% C.L. limits on diffuse UHE gamma ray fluxes, in comparison with other experiments and models (see [40, 41] and references therein). Right: 90% C.L. limits on diffuse UHE neutrino fluxes, shown in integrated (lines) and differential forms, compared with models and other observatories (see [42, 43] and references therein).

expectations from the matter distribution of the large-scale structure [37]. Simulations further show that defining light and heavy cosmic-ray populations through a universality- or DNN-based mass estimators enables the study of dipole behavior in mass-selective subsamples as shown in Fig. 11 (right) [38]. Such an analysis may reveal a measurable separation in the dipole amplitude between light and heavy primary components.

The possible sky regions of origin for the highest-energy cosmic rays observed during Phase I of the Pierre Auger Observatory were reconstructed through Galactic backtracking with constraints on maximum propagation distance, employing both a single-event analysis and a likelihood-based approach [39]. The single-event study shows that all but one event have at least one plausible astrophysical counterpart within the 95% CL localization region, with the event PAO180812 gaining plausible associations only when a 14% systematic energy shift is applied. The likelihood analysis further indicates that most tested source catalogs are incompatible as dominant contributors above 100 EeV, suggesting that multiple source classes, significant EGMF deflections, or a contribution from ultra-heavy nuclei may be required.

3.4 Multimessenger astrophysics

Cosmogenic particles originate from interactions between the highest-energy cosmic rays and background photon fields, making them valuable probes of ultra-high-energy cosmic-ray physics. Improved sensitivity to neutrinos and photons will enhance our ability to constrain properties of UHECR sources, including their cosmological evolution [44]. Such sensitivity is also central to multimessenger analyses, particularly in searches for point-like sources in both space and time. These searches include correlations with transient astrophysical objects, such as binary neutron star mergers studied in [45, 46].

Limits on neutrino and photon fluxes as shown in Fig. 12 additionally provide a means to test extensions of the Standard Model of Particle Physics. For example, they allow investigations of Lorentz invariance violation in extragalactic particle propagation [49]. They also contribute to
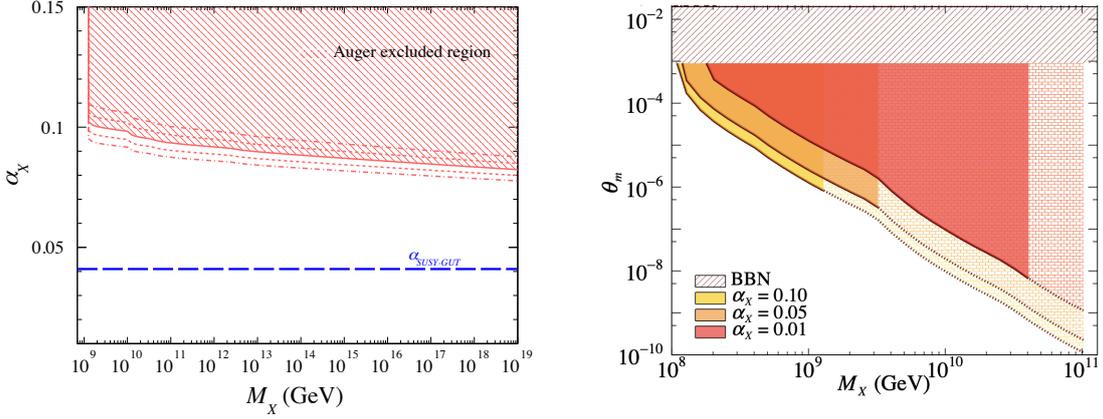
Figure 13: The left panel shows the 95% C.L. upper limits on the hidden-gauge coupling constant α_X as a function of the dark-matter particle mass M_X, assuming that X constitutes the full dark-matter abundance and decays into multiple $\bar{q}q$ pairs [47]. The right panel presents the constraints on θ_m versus M_X for three choices of α_X with $\lambda_{N_m} = 10^{-5}$, where the hatched red region $\theta_m \geq 9 \times 10^{-4}$ is excluded by limits on ΔN_{eff} [48] (N_m being the number of sterile neutrinos and N_{eff} the effective neutrino number).

constraining possible dark matter scenarios and interactions [47, 48] as shown in Fig. 13. Beyond flux limits, the ability to detect upward-going air showers offers another channel for probing non-standard physics [50, 51]. Furthermore, sensitivity to details of the shower development enables tests of Lorentz invariance violation within extensive air showers themselves [52]. Altogether, cosmogenic particles serve as a crucial bridge between UHECR observations, multimessenger astrophysics, and searches for new physics.

4. The astrophysical picture

The experimental results challenge traditional astrophysical scenarios, particularly the long-favored proton paradigm for ultra-high-energy cosmic rays (UHECRs). These measurements reveal an unexpected astrophysical picture in which the energy evolution of the X_{max} distribution characteristics, particularly $\sigma(X_{\text{max}})$, indicates that only a very limited mixture of nuclear species can reach Earth. This, in turn, implies that UHECR nuclei must be emitted from their sources with nearly monochromatic spectra, tightly constraining viable source scenarios.

Such behavior is compatible with hard power-law source spectra and low-rigidity cutoffs above the ankle, with minimal source-to-source variation, cf. Fig. 14 and Ref. [53], where a low-energy extragalactic light population with a soft spectrum at source describes the low energy tail. The high-energy flux suppression would then stem from both propagation effects and the finite acceleration power of sources. The contrast between the hard spectral index above the ankle and the much softer one below it may arise from particle confinement in the source environment. In-source interactions can further dictate the ordering of mass fractions at escape, influencing the observed ordering at Earth. The hardness of the source spectrum above the ankle should not be directly compared with expectations from Fermi acceleration because the modeled spectra describe escape rather than acceleration. Identifying the proton fraction is essential for interpreting cosmogenic
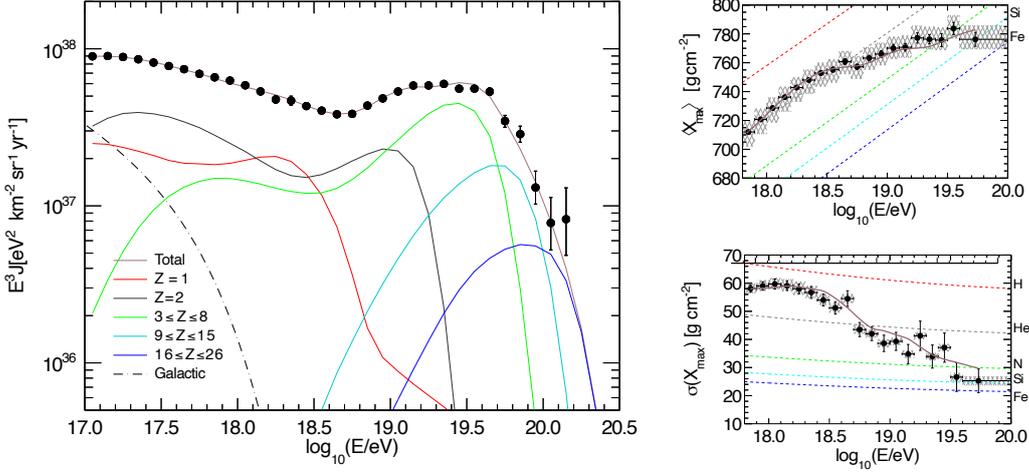
Figure 14: Results of the combined fit to the energy spectrum ($E \geq 10^{17}$ eV) and to the $X_{\max}$ moments ($E \geq 10^{17.8}$ eV) using the hadronic interaction model Sibyll 2.3d with a shape parameter $\Delta = 2$ describing the falloff of the rigidity cutoff (see Ref. [53] for details).

particle production and assessing in-source interaction efficiencies. Determining the mass fractions of the heaviest nuclei at the highest energies is therefore a central objective of Phase II of the Pierre Auger Observatory, as it is key to uncovering the nature of UHECR sources [18, 53].

5. The road ahead

To illustrate the potential of Phase II, a preliminary energy spectrum based solely on Phase II data was presented at the conference. The spectrum was derived from vertical Phase-II events recorded between April 1, 2023 and March 1, 2025. It was reconstructed entirely using the Phase-I analysis framework, as shown in Fig. 15. This reuse of the original procedure including the lateral distribution function, attenuation with zenith-angle, energy calibration, and detector response was enabled by the backward compatibility of the upgraded Water-Cherenkov Detectors. The resulting Phase-II exposure is $(9200 \pm 300)\,\text{km}^2\,\text{sr}\,\text{yr}$, approximately 10% of the Phase-I exposure. A statistical analysis of the Phase-I and Phase-II spectra indicate consistency between the two datasets [16]. Fitting the Phase-II spectrum with the Phase-I model produces spectral parameters compatible within statistical uncertainties. Overall, this early analysis shows that only minor modifications to the reconstruction will be required before combining Phase-I and Phase-II data into a single, full-exposure spectrum.

AugerPrime is now fully operational and the final steps of commissioning its physics data sets are under way, marking the start of a new analysis era. The upgrade enables mass-sensitive studies of anisotropies in the arrival directions of ultra-high-energy cosmic rays in a multi-hybrid fashion [9] and also provides significantly improved precision for testing and constraining hadronic interaction models. With the enhanced capabilities, the mass composition of UHECRs can be probed to energies beyond the observed break due to the suppression in the spectrum. In parallel, the experiment is expected to deliver either direct measurements or markedly tighter limits on neutral
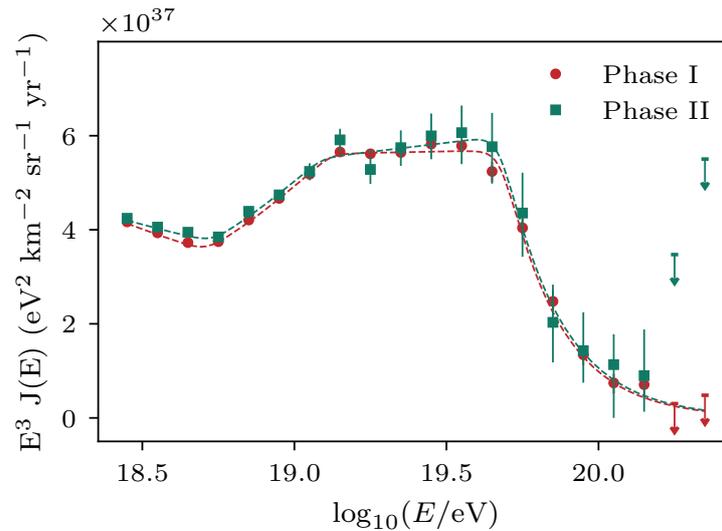
Figure 15: Preliminary spectrum using events arriving with zenith angle up to 60° recorded in Phase II (green markers). The spectrum of Phase I is displayed for comparison (red markers) [16].

particles, while expanding searches for physics beyond the Standard Model. The rich Phase-II data set, together with a more reliable mass-scale calibration, will allow refined investigations of the various components of extensive air showers. Finally, the insights gained from AugerPrime will be applied to a re-analysis of the Phase-I data, further strengthening the overall scientific reach of the Observatory.

The wealth of scientific findings is not limited to the results discussed here. Further investigations covering other areas of research such as cosmogeophysics [54], space weather [55], outreach [56] or the development of new detectors (see e.g. [57, 58]) make the Observatory a long-term scientific flagship facility that extends far beyond astroparticle physics.

References

[1] R. Aloisio, V. Berezinsky and A. Gazizov, *Astropart. Phys.* **34** (2011) 620 [0907.5194].

[2] K. Greisen, *Phys. Rev. Lett.* **16** (1966) 748.

[3] G.T. Zatsepin and V.A. Kuzmin, *JETP Lett.* **4** (1966) 78.

[4] Pierre Auger Collaboration, *Phys. Rev. D* **91** (2015) 032003 [1408.1421].

[5] Pierre Auger Collaboration, *Phys. Rev. Lett.* **117** (2016) 192001 [1610.08509].

[6] Pierre Auger Collaboration, *Eur. Phys. J. C* **80** (2020) 751.

[7] Pierre Auger Collaboration, *Phys. Rev. Lett.* **126** (2021) 152002 [2102.07797].

[8] Jakub Vicha for the Pierre Auger Collaboration, *PoS* **ICRC2025** (2025) 431 [2507.09802].

[9] David Schmidt for the Pierre Auger Collaboration, *PoS* **ICRC2025** (2025) 385 [2508.08056].

[10] Denise Boncioli for the Pierre Auger Collaboration, *PoS* **UHECR2024** (2025) 027 [2509.15862].

[11] Olivier Deligny for the Pierre Auger Collaboration in *Proceedings of EPS-HEP 2025*, July, 2025.

[12] Ingomar Allekotte for the Pierre Auger Collaboration and Alejandra Calvo, *PoS* **ICRC2025** (2025) 1236.

[13] Pierre Auger Collaboration, 1604.03637.

[14] Pierre Auger Collaboration, *Astrophys. J. Suppl.* **264** (2023) 50 [2211.16020].

[15] Pierre Auger Collaboration, 2506.11688.

[16] Diegeo Ravignani for the Auger Collaboration, *PoS* **ICRC2025** (2025) 370 [2507.08573].

[17] Pierre Auger Collaboration, *Phys. Rev. D* **102** (2020) 062005 [2008.06486].

[18] Eric Mayotte for the Pierre Auger Collaboration, *PoS* **ICRC2023** (2023) 365.

[19] Maximilian Stadelmaier for the Pierre Auger Collaboration, *PoS* **UHECR2024** (2025) 117.

[20] Pedro Abreu for the Pierre Auger Collaboration, *PoS* **ICRC2023** (2023) 319.

[21] Pierre Auger Collaboration, *Phys. Rev. D* **90** (2014) 122005 [1409.4809].

[22] Eric Mayotte for the Pierre Auger Collaboration, *PoS* **ICRC2025** (2025) 331 [2507.10292].

[23] Pierre Auger Collaboration, *Phys. Rev. D* **111** (2025) 022003 [2406.06319].

[24] Pierre Auger Collaboration, *Phys. Rev. D, in preparation* (2026) .

[25] Pierre Auger Collaboration, *Phys. Rev. D* **109** (2024) 022002 [2310.19966].

[26] Pierre Auger Collaboration, *Phys. Rev. Lett.* **132** (2024) 021001 [2310.19963].

[27] Jose Bellido for the Pierre Auger Collaboration, *PoS* **ICRC2017** (2018) 506.

[28] Maximilian Stadelmaier for the Pierre Auger Collaboration, *PoS* **ICRC2025** (2025) 426 [2507.13209].

[29] Pierre Auger Collaboration, *JCAP* **02** (2013) 026 [1301.6637].

[30] Pierre Auger Collaboration, *Phys. Rev. D* **90** (2014) 122006 [1409.5083].

[31] T. Pierog, *PoS* **ICRC2017** (2018) 1100.

[32] F. Riehn, H.P. Dembinski, R. Engel et al., *PoS* **ICRC2017** (2018) 301 [1709.07227].

[33] S. Ostapchenko, *Phys. Rev. D* **83** (2011) 014018 [1010.1869].

[34] Olena Tkachenko for the Auger Collaboration, *PoS* (2025) 431 [2507.19326].

[35] Pierre Auger Collaboration, *Phys. Rev. D* **109** (2024) 102001 [2401.10740].

[36] Pierre Auger Collaboration, *Astrophys. J.* **935** (2022) 170 [2206.13492].

[37] Pierre Auger Collaboration, *Astrophys. J.* **976** (2024) 48 [2408.05292].

[38] Garaldina Golup for the Pierre Auger Collaboration, *PoS* **ICRC2025** (2025) 272 [2507.08564].

[39] Marta Bianciotto for the Pierre Auger Collaboration, *PoS* **ICRC2025** (2025) 195 [2507.19216].

[40] Pierpaolo Savina for the Auger Collaboration, *PoS* **ICRC2025** (2025) 965 [2509.05113].

[41] Pierre Auger Collaboration, *JCAP* **05** (2025) 061 [2502.02381].

[42] Srijan Sehgal for the Pierre Auger Collaboration, *PoS* **ICRC2025** (2025) 1170 [2507.10214].

[43] Pierre Auger Collaboration, *JCAP* **10** (2019) 022 [1906.07422].

[44] Camilla Petrucci for the Pierre Auger Collaboration, *PoS* **ICRC2023** (2023) 1520.

[45] LIGO Scientific, et al. Collaboration, *Astrophys. J. Lett.* **848** (2017) L12 [1710.05833].

[46] ANTARES, IceCube, Pierre Auger, LIGO Scientific, Virgo Collaboration, *Astrophys. J. Lett.* **850** (2017) L35 [1710.05839].

[47] Pierre Auger Collaboration, *Phys. Rev. Lett.* **130** (2023) 061001 [2203.08854].

[48] Pierre Auger Collaboration, *Phys. Rev. D* **109** (2024) L081101 [2311.14541].

[49] Pierre Auger Collaboration, *JCAP* **01** (2022) 023 [2112.06773].

[50] Emanuele de Vito for the Pierre Auger Collaboration, *PoS* **ICRC2023** (2023) 1099.

[51] Baobiao Yue for the Pierre Auger Collaboration, *PoS* **ICRC2023** (2023) 1095.

[52] Caterina Trimarelli for the Pierre Auger Collaboration, *PoS* **ICRC2021** (2021) 340.

[53] Esteban Roulet for the Pierre Auger Collaboration, *PoS* **ICRC2025** (2025) 373 [2507.10806].

[54] Roberto Mussa for the Pierre Auger Collaboration, *PoS* **ICRC2025** (2025) 342 [2507.11641].

[55] Carla Taricco for the Pierre Auger Collaboration and I. Bizzarri, C. Dionese, and S. Mancuso, *PoS* **ICRC2025** (2025) 1370 [2510.20589].

[56] Fabio Convenga for the Pierre Auger Collaboration, *PoS* **ICRC2025** (2025) 1242 [2509.11850].

[57] Stef Verpoest et al. for the IceCube-Gen2 and Pierre Auger Collaborations, *PoS* **ICRC2025** (2025) 428 [2507.08991].

[58] Adriel Bartz-Mocellin for the Pierre Auger Collaboration, *PoS* **ICRC2025** (2025) 182.

16

The Pierre Auger Collaboration

A. Abdul Halim[13], P. Abreu[70], M. Aglietta[53,51], I. Allekotte[1], K. Almeida Cheminant[78,77], A. Almela[7,12], R. Aloisio[44,45], J. Alvarez-Muñiz[76], A. Ambrosone[44], J. Ammerman Yebra[76], G.A. Anastasi[57,46], L. Anchordoqui[83], B. Andrada[7], L. Andrade Dourado[44,45], S. Andringa[70], L. Apollonio[58,48], C. Aramo[49], E. Arnone[62,51], J.C. Arteaga Velázquez[66], P. Assis[70], G. Avila[11], E. Avocone[56,45], A. Bakalova[31], F. Barbato[44,45], A. Bartz Mocellin[82], J.A. Bellido[13], C. Berat[35], M.E. Bertaina[62,51], M. Bianciotto[62,51], P.L. Biermann[a], V. Binet[5], K. Bismark[38,7], T. Bister[77,78], J. Biteau[36,i], J. Blazek[31], J. Blümer[40], M. Boháčová[31], D. Boncioli[56,45], C. Bonifazi[8], L. Bonneau Arbeletche[22], N. Borodai[68], J. Brack[f], P.G. Brichetto Orchera[7,40], F.L. Briechle[41], A. Bueno[75], S. Buitink[15], M. Buscemi[46,57], M. Büsken[38,7], A. Bwembya[77,78], K.S. Caballero-Mora[65], S. Cabana-Freire[76], L. Caccianiga[58,48], F. Campuzano[6], J. Caraça-Valente[82], R. Caruso[57,46], A. Castellina[53,51], F. Catalani[19], G. Cataldi[47], L. Cazon[76], M. Cerda[10], B. Čermáková[40], A. Cermenati[44,45], J.A. Chinellato[22], J. Chudoba[31], L. Chytka[32], R.W. Clay[13], A.C. Cobos Cerutti[6], R. Colalillo[59,49], R. Conceição[70], G. Consolati[48,54], M. Conte[55,47], F. Convenga[44,45], D. Correia dos Santos[27], P.J. Costa[70], C.E. Covault[81], M. Cristinziani[43], C.S. Cruz Sanchez[3], S. Dasso[4,2], K. Daumiller[40], B.R. Dawson[13], R.M. de Almeida[27], E.-T. de Boone[43], B. de Errico[27], J. de Jesús[7], S.J. de Jong[77,78], J.R.T. de Mello Neto[27], I. De Mitri[44,45], J. de Oliveira[18], D. de Oliveira Franco[42], F. de Palma[55,47], V. de Souza[20], E. De Vito[55,47], A. Del Popolo[57,46], O. Deligny[33], N. Denner[31], L. Deval[53,51], A. di Matteo[51], C. Dobrigkeit[22], J.C. D'Olivo[67], L.M. Domingues Mendes[16,70], Q. Dorosti[43], J.C. dos Anjos[16], R.C. dos Anjos[26], J. Ebr[31], F. Ellwanger[40], R. Engel[38,40], I. Epicoco[55,47], M. Erdmann[41], A. Etchegoyen[7,12], C. Evoli[44,45], H. Falcke[77,79,78], G. Farrar[85], A.C. Fauth[22], T. Fehler[43], F. Feldbusch[39], A. Fernandes[70], M. Fernandez[14], B. Fick[84], J.M. Figueira[7], P. Filip[38,7], A. Filipčič[74,73], T. Fitoussi[40], B. Flaggs[87], T. Fodran[77], A. Franco[47], M. Freitas[70], T. Fujii[86,h], A. Fuster[7,12], C. Galea[77], B. García[6], C. Gaudu[37], P.L. Ghia[33], U. Giaccari[47], F. Gobbi[10], F. Gollan[7], G. Golup[1], M. Gómez Berisso[1], P.F. Gómez Vitale[11], J.P. Gongora[11], J.M. González[1], N. González[7], D. Góra[68], A. Gorgi[53,51], M. Gottowik[40], F. Guarino[59,49], G.P. Guedes[23], L. Gülzow[40], S. Hahn[38], P. Hamal[31], M.R. Hampel[7], P. Hansen[3], V.M. Harvey[13], A. Haungs[40], T. Hebbeker[41], C. Hojvat[d], J.R. Hörandel[77,78], P. Horvath[32], M. Hrabovský[32], T. Huege[40,15], A. Insolia[57,46], P.G. Isar[72], M. Ismaiel[77,78], P. Janecek[31], V. Jilek[31], K.-H. Kampert[37], B. Keilhauer[40], A. Khakurdikar[77], V.V. Kizakke Covilakam[7,40], H.O. Klages[40], M. Kleifges[39], J. Köhler[40], F. Krieger[41], M. Kubatova[31], N. Kunka[39], B.L. Lago[17], N. Langner[41], N. Leal[7], M.A. Leigui de Oliveira[25], Y. Lema-Capeans[76], A. Letessier-Selvon[34], I. Lhenry-Yvon[33], L. Lopes[70], J.P. Lundquist[73], M. Mallamaci[60,46], D. Mandat[31], P. Mantsch[d], F.M. Mariani[58,48], A.G. Mariazzi[3], I.C. Mariş[14], G. Marsella[60,46], D. Martello[55,47], S. Martinelli[40,7], M.A. Martins[76], H.-J. Mathes[40], J. Matthews[g], G. Matthiae[61,50], E. Mayotte[82], S. Mayotte[82], P.O. Mazur[d], G. Medina-Tanco[67], J. Meinert[37], D. Melo[7], A. Menshikov[39], C. Merx[40], S. Michal[31], M.I. Micheletti[5], L. Miramonti[58,48], M. Mogarkar[68], S. Mollerach[1], F. Montanet[35], L. Morejon[37], K. Mulrey[77,78], R. Mussa[51], W.M. Namasaka[37], S. Negi[31], L. Nellen[67], K. Nguyen[84], G. Nicora[9], M. Niechciol[43], D. Nitz[84], D. Nosek[30], A. Novikov[87], V. Novotny[30], L. Nožka[32], A. Nucita[55,47], L.A. Núñez[29], J. Ochoa[7,40], C. Oliveira[20], L. Östman[31], M. Palatka[31], J. Pallotta[9], S. Panja[31], G. Parente[76], T. Paulsen[37], J. Pawlowsky[37], M. Pech[31], J. Pękala[68], R. Pelayo[64], V. Pelgrims[14], L.A.S. Pereira[24], E.E. Pereira Martins[38,7], C. Pérez Bertolli[7,40], L. Perrone[55,47], S. Petrera[44,45], C. Petrucci[56], T. Pierog[40], M. Pimenta[70], M. Platino[7], B. Pont[77], M. Pourmohammad Shahvar[60,46], P. Privitera[86], C. Priyadarshi[68], M. Prouza[31], K. Pytel[69], S. Querchfeld[37], J. Rautenberg[37], D. Ravignani[7], J.V. Reginatto Akim[22], A. Reuzki[41], J. Ridky[31], F. Riehn[76,j], M. Risse[43], V. Rizi[56,45], E. Rodriguez[7,40], G. Rodriguez Fernandez[50], J. Rodriguez Rojo[11], S. Rossoni[42], M. Roth[40], E. Roulet[1], A.C. Rovero[4], A. Saftoiu[71], M. Saharan[77], F. Salamida[56,45], H. Salazar[63], G. Salina[50], P. Sampathkumar[40], N. San Martin[82], J.D. Sanabria Gomez[29], F. Sánchez[7], E.M. Santos[21], E. Santos[31], F. Sarazin[82], R. Sarmento[70], R. Sato[11], P. Savina[44,45], V. Scherini[55,47], H. Schieler[40], M. Schimassek[33], M. Schimp[37], D. Schmidt[40], O. Scholten[15,b], H. Schoorlemmer[77,78], P. Schovánek[31], F.G. Schröder[87,40], J. Schulte[41], T. Schulz[31], S.J. Sciutto[3], M. Scornavacche[7], A. Sedoski[7], A. Segreto[52,46], S. Sehgal[37], S.U. Shivashankara[73], G. Sigl[42], K. Simkova[15,14], F. Simon[39], R. Šmída[86], P. Sommers[e], R. Squartini[10], M. Stadelmaier[40,48,58], S. Stanič[73], J. Stasielak[68], P. Stassi[35], S. Strähnz[38], M. Straub[41], T. Suomijärvi[36], A.D. Supanitsky[7], Z. Svozilikova[31], K. Syrokvas[30], Z. Szadkowski[69], F. Tairli[13], M. Tambone[59,49], A. Tapia[28], C. Taricco[62,51], C. Timmermans[78,77], O. Tkachenko[31], P. Tobiska[31], C.J. Todero Peixoto[19], B. Tomé[70], A. Travaini[10], P. Travnicek[31], M. Tueros[3], M. Unger[40], R. Uzeiroska[37], L. Vaclavek[32], M. Vacula[32], I. Vaiman[44,45], J.F. Valdés Galicia[67], L. Valore[59,49], P. van Dillen[77,78], E. Varela[63], V. Vašíčková[37], A. Vásquez-Ramírez[29], D. Veberič[40], I.D. Vergara Quispe[3], S. Verpoest[87], V. Verzi[50], J. Vicha[31], J. Vink[80], S. Vorobiov[73], J.B. Vuta[31], C. Watanabe[27], A.A. Watson[c], A. Weindl[40], M. Weitz[37], L. Wiencke[82], H. Wilczyński[68], B. Wundheiler[7], B. Yue[37], A. Yushkov[31], E. Zas[76], D. Zavrtanik[73,74], M. Zavrtanik[74,73]

17

[1] Centro Atómico Bariloche and Instituto Balseiro (CNEA-UNCuyo-CONICET), San Carlos de Bariloche, Argentina

[2] Departamento de Física and Departamento de Ciencias de la Atmósfera y los Océanos, FCEyN, Universidad de Buenos Aires and CONICET, Buenos Aires, Argentina

[3] IFLP, Universidad Nacional de La Plata and CONICET, La Plata, Argentina

[4] Instituto de Astronomía y Física del Espacio (IAFE, CONICET-UBA), Buenos Aires, Argentina

[5] Instituto de Física de Rosario (IFIR) – CONICET/U.N.R. and Facultad de Ciencias Bioquímicas y Farmacéuticas U.N.R., Rosario, Argentina

[6] Instituto de Tecnologías en Detección y Astropartículas (CNEA, CONICET, UNSAM), and Universidad Tecnológica Nacional – Facultad Regional Mendoza (CONICET/CNEA), Mendoza, Argentina

[7] Instituto de Tecnologías en Detección y Astropartículas (CNEA, CONICET, UNSAM), Buenos Aires, Argentina

[8] International Center of Advanced Studies and Instituto de Ciencias Físicas, ECyT-UNSAM and CONICET, Campus Miguelete – San Martín, Buenos Aires, Argentina

[9] Laboratorio Atmósfera – Departamento de Investigaciones en Láseres y sus Aplicaciones – UNIDEF (CITEDEF-CONICET), Argentina

[10] Observatorio Pierre Auger, Malargüe, Argentina

[11] Observatorio Pierre Auger and Comisión Nacional de Energía Atómica, Malargüe, Argentina

[12] Universidad Tecnológica Nacional – Facultad Regional Buenos Aires, Buenos Aires, Argentina

[13] University of Adelaide, Adelaide, S.A., Australia

[14] Université Libre de Bruxelles (ULB), Brussels, Belgium

[15] Vrije Universiteit Brussels, Brussels, Belgium

[16] Centro Brasileiro de Pesquisas Fisicas, Rio de Janeiro, RJ, Brazil

[17] Centro Federal de Educação Tecnológica Celso Suckow da Fonseca, Petropolis, Brazil

[18] Instituto Federal de Educação, Ciência e Tecnologia do Rio de Janeiro (IFRJ), Brazil

[19] Universidade de São Paulo, Escola de Engenharia de Lorena, Lorena, SP, Brazil

[20] Universidade de São Paulo, Instituto de Física de São Carlos, São Carlos, SP, Brazil

[21] Universidade de São Paulo, Instituto de Física, São Paulo, SP, Brazil

[22] Universidade Estadual de Campinas (UNICAMP), IFGW, Campinas, SP, Brazil

[23] Universidade Estadual de Feira de Santana, Feira de Santana, Brazil

[24] Universidade Federal de Campina Grande, Centro de Ciencias e Tecnologia, Campina Grande, Brazil

[25] Universidade Federal do ABC, Santo André, SP, Brazil

[26] Universidade Federal do Paraná, Setor Palotina, Palotina, Brazil

[27] Universidade Federal do Rio de Janeiro, Instituto de Física, Rio de Janeiro, RJ, Brazil

[28] Universidad de Medellín, Medellín, Colombia

[29] Universidad Industrial de Santander, Bucaramanga, Colombia

[30] Charles University, Faculty of Mathematics and Physics, Institute of Particle and Nuclear Physics, Prague, Czech Republic

[31] Institute of Physics of the Czech Academy of Sciences, Prague, Czech Republic

[32] Palacky University, Olomouc, Czech Republic

[33] CNRS/IN2P3, IJCLab, Université Paris-Saclay, Orsay, France

[34] Laboratoire de Physique Nucléaire et de Hautes Energies (LPNHE), Sorbonne Université, Université de Paris, CNRS-IN2P3, Paris, France

[35] Univ. Grenoble Alpes, CNRS, Grenoble Institute of Engineering Univ. Grenoble Alpes, LPSC-IN2P3, 38000 Grenoble, France

[36] Université Paris-Saclay, CNRS/IN2P3, IJCLab, Orsay, France

[37] Bergische Universität Wuppertal, Department of Physics, Wuppertal, Germany

[38] Karlsruhe Institute of Technology (KIT), Institute for Experimental Particle Physics, Karlsruhe, Germany

[39] Karlsruhe Institute of Technology (KIT), Institut für Prozessdatenverarbeitung und Elektronik, Karlsruhe, Germany

[40] Karlsruhe Institute of Technology (KIT), Institute for Astroparticle Physics, Karlsruhe, Germany

[41] RWTH Aachen University, III. Physikalisches Institut A, Aachen, Germany

[42] Universität Hamburg, II. Institut für Theoretische Physik, Hamburg, Germany

[43] Universität Siegen, Department Physik – Experimentelle Teilchenphysik, Siegen, Germany

[44] Gran Sasso Science Institute, L'Aquila, Italy

[45] INFN Laboratori Nazionali del Gran Sasso, Assergi (L'Aquila), Italy

[46] INFN, Sezione di Catania, Catania, Italy

[47] INFN, Sezione di Lecce, Lecce, Italy

[48] INFN, Sezione di Milano, Milano, Italy

[49] INFN, Sezione di Napoli, Napoli, Italy

[50] INFN, Sezione di Roma "Tor Vergata", Roma, Italy

[51] INFN, Sezione di Torino, Torino, Italy

52 Istituto di Astrofisica Spaziale e Fisica Cosmica di Palermo (INAF), Palermo, Italy
53 Osservatorio Astrofisico di Torino (INAF), Torino, Italy
54 Politecnico di Milano, Dipartimento di Scienze e Tecnologie Aerospaziali , Milano, Italy
55 Università del Salento, Dipartimento di Matematica e Fisica "E. De Giorgi", Lecce, Italy
56 Università dell'Aquila, Dipartimento di Scienze Fisiche e Chimiche, L'Aquila, Italy
57 Università di Catania, Dipartimento di Fisica e Astronomia "Ettore Majorana", Catania, Italy
58 Università di Milano, Dipartimento di Fisica, Milano, Italy
59 Università di Napoli "Federico II", Dipartimento di Fisica "Ettore Pancini", Napoli, Italy
60 Università di Palermo, Dipartimento di Fisica e Chimica "E. Segrè", Palermo, Italy
61 Università di Roma "Tor Vergata", Dipartimento di Fisica, Roma, Italy
62 Università Torino, Dipartimento di Fisica, Torino, Italy
63 Benemérita Universidad Autónoma de Puebla, Puebla, México
64 Unidad Profesional Interdisciplinaria en Ingeniería y Tecnologías Avanzadas del Instituto Politécnico Nacional (UPIITA-IPN), México, D.F., México
65 Universidad Autónoma de Chiapas, Tuxtla Gutiérrez, Chiapas, México
66 Universidad Michoacana de San Nicolás de Hidalgo, Morelia, Michoacán, México
67 Universidad Nacional Autónoma de México, México, D.F., México
68 Institute of Nuclear Physics PAN, Krakow, Poland
69 University of Łódź, Faculty of High-Energy Astrophysics,Łódź, Poland
70 Laboratório de Instrumentação e Física Experimental de Partículas – LIP and Instituto Superior Técnico – IST, Universidade de Lisboa – UL, Lisboa, Portugal
71 "Horia Hulubei" National Institute for Physics and Nuclear Engineering, Bucharest-Magurele, Romania
72 Institute of Space Science, Bucharest-Magurele, Romania
73 Center for Astrophysics and Cosmology (CAC), University of Nova Gorica, Nova Gorica, Slovenia
74 Experimental Particle Physics Department, J. Stefan Institute, Ljubljana, Slovenia
75 Universidad de Granada and C.A.F.P.E., Granada, Spain
76 Instituto Galego de Física de Altas Enerxías (IGFAE), Universidade de Santiago de Compostela, Santiago de Compostela, Spain
77 IMAPP, Radboud University Nijmegen, Nijmegen, The Netherlands
78 Nationaal Instituut voor Kernfysica en Hoge Energie Fysica (NIKHEF), Science Park, Amsterdam, The Netherlands
79 Stichting Astronomisch Onderzoek in Nederland (ASTRON), Dwingeloo, The Netherlands
80 Universiteit van Amsterdam, Faculty of Science, Amsterdam, The Netherlands
81 Case Western Reserve University, Cleveland, OH, USA
82 Colorado School of Mines, Golden, CO, USA
83 Department of Physics and Astronomy, Lehman College, City University of New York, Bronx, NY, USA
84 Michigan Technological University, Houghton, MI, USA
85 New York University, New York, NY, USA
86 University of Chicago, Enrico Fermi Institute, Chicago, IL, USA
87 University of Delaware, Department of Physics and Astronomy, Bartol Research Institute, Newark, DE, USA

—

a Max-Planck-Institut für Radioastronomie, Bonn, Germany
b also at Kapteyn Institute, University of Groningen, Groningen, The Netherlands
c School of Physics and Astronomy, University of Leeds, Leeds, United Kingdom
d Fermi National Accelerator Laboratory, Fermilab, Batavia, IL, USA
e Pennsylvania State University, University Park, PA, USA
f Colorado State University, Fort Collins, CO, USA
g Louisiana State University, Baton Rouge, LA, USA
h now at Graduate School of Science, Osaka Metropolitan University, Osaka, Japan
i Institut universitaire de France (IUF), France
j now at Technische Universität Dortmund and Ruhr-Universität Bochum, Dortmund and Bochum, Germany

Acknowledgments